

ARTICLE

Open Access

# Facet nanoarchitectonics of visible-light driven $\text{Ag}_3\text{PO}_4$ photocatalytic micromotors: Tuning motion for biofilm eradication

Daniel Rojas<sup>1</sup>, Michaela Kuthanova<sup>2</sup>, Kristyna Dolezelikova<sup>2</sup> and Martin Pumera<sup>1,3,4,5</sup> 

## Abstract

The customized design of micro-/nanomotors represents one of the main research topics in the field of micro-/nanomotors; however, the effects of different crystal facets on micromotor movement are often neglected. In this work, self-propelled amorphous, cubic, and tetrahedral  $\text{Ag}_3\text{PO}_4$  particles were synthesized using a scalable precipitation method. Their programmable morphologies exhibited different motion properties under fuel-free and surfactant-free conditions and visible light irradiation. Differences in these motion properties were observed according to morphology and correlated with photocatalytic activity. Moreover,  $\text{Ag}_3\text{PO}_4$  micromotors are inherently fluorescent, which allows fluorescence-based tracking. Furthermore, bacterial biofilms represent a major concern in modern society since most of them are antibiotic resistant. The as-prepared self-propelled particles exhibited morphologically dependent antibiofilm activities toward gram-positive and gram-negative bacteria. The enhanced diffusion of the particles promoted biofilm removal in comparison with static control experiments, realizing the possibility of a new class of light-driven biofilm-eradicating micromotors that do not require the use of both  $\text{H}_2\text{O}_2$  and UV light.

## Introduction

Light-driven nano-/micromotors have received great attention in recent years due to their interesting advantages compared to catalytic micromotors. The use of light to drive motion allows remote action in their movements, reversible on/off motion and the tuning of active wavelengths by tuning the micromotor composition, which are difficult to obtain in chemically driven micromotors<sup>1</sup>. Hence, there is increasing interest in the synthesis and characterization of light-active materials as nano-/micromotors. For instance,  $\text{TiO}_2$ <sup>2,3</sup>,  $\text{ZnO}$ <sup>4</sup>, and  $\text{AgCl}$ <sup>5,6</sup> have been used as photoactive materials under UV irradiation. However, there is growing interest in developing new nanomaterials that are capable of producing motion

under visible light irradiation, such as  $\text{Cu}_2\text{O}$ <sup>7</sup>,  $\text{SiO}_2/\text{Au}/\text{PEN}$ <sup>8</sup>, and  $\text{BiVO}_4$ <sup>9</sup>, sulfur- and nitrogen-containing porous donor–acceptor polymers (SNPs)<sup>10</sup> or  $\text{C}_3\text{N}_4$ <sup>11</sup>.  $\text{Ag}_3\text{PO}_4$  is a promising photocatalytic material due to its high separation of photogenerated electron/hole pairs facilitated by the absorption of visible light. This enables the degradation of organic pollutants and the production of oxygen from water splitting. Different strategies for improving  $\text{Ag}_3\text{PO}_4$  photoactivity have been reported, such as its combination with other materials to form composites or heterostructures and in crystal facet engineering<sup>12</sup>. Despite its promising capabilities as a visible-light driven photocatalyst, it has been scarcely used for the development of micromotors.  $\text{Ag}_3\text{PO}_4$  micromotors have been proposed as active colloids using UV light<sup>13</sup> or chemical<sup>14</sup> stimuli in their spherical form containing mixed facets and as visible light-driven micromotors in their cubic form<sup>15</sup>. The controllable synthesis of light-driven micromotors is still a relevant area of research in the field of improving micromotor capabilities. In recent years,

Correspondence: Martin Pumera ([pumera.research@gmail.com](mailto:pumera.research@gmail.com))

<sup>1</sup>Future Energy and Innovation Laboratory, Central European Institute of Technology, Brno University of Technology (CEITEC-BUT), Purkyňova 123, 61200 Brno, Czech Republic

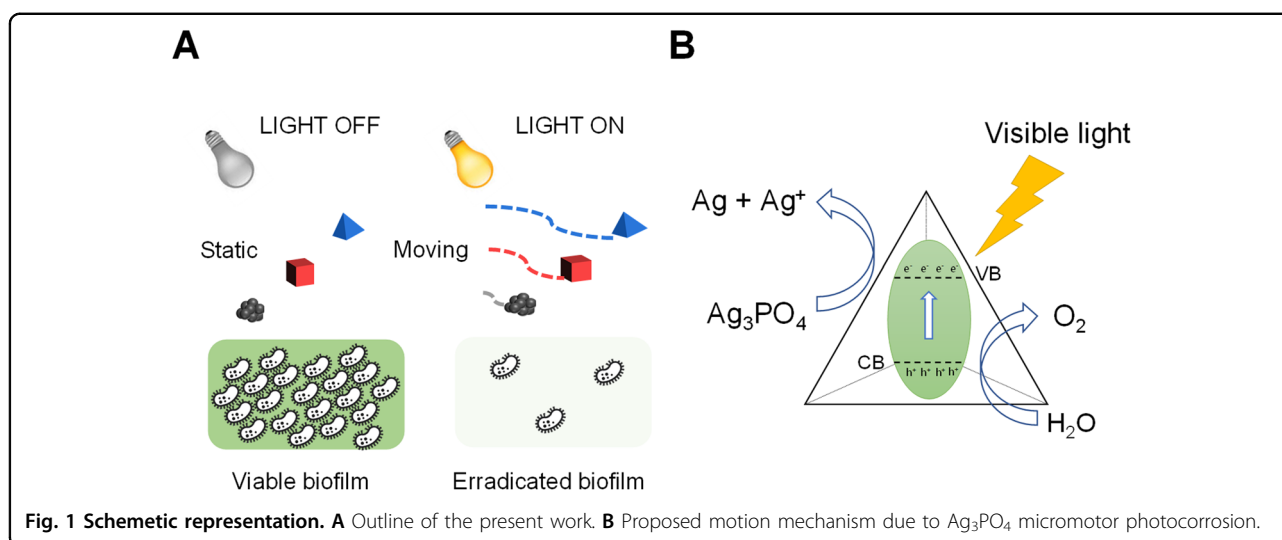
<sup>2</sup>Department of Chemistry and Biochemistry, Mendel University in Brno, Zemedelska 1, CZ-613 00 Brno, Czech Republic

Full list of author information is available at the end of the article

© The Author(s) 2022



**Open Access** This article is licensed under a Creative Commons Attribution 4.0 International License, which permits use, sharing, adaptation, distribution and reproduction in any medium or format, as long as you give appropriate credit to the original author(s) and the source, provide a link to the Creative Commons license, and indicate if changes were made. The images or other third party material in this article are included in the article's Creative Commons license, unless indicated otherwise in a credit line to the material. If material is not included in the article's Creative Commons license and your intended use is not permitted by statutory regulation or exceeds the permitted use, you will need to obtain permission directly from the copyright holder. To view a copy of this license, visit <http://creativecommons.org/licenses/by/4.0/>.



different structures, such as microtubes<sup>11,16</sup> and Janus spheres<sup>17–19</sup>, have been successfully implemented in micro-/nanorobots using different catalytic materials. However, even considering the critical role that facets have in the photocatalytic performance of a semiconductor, it remains unexplored in the micromotor field except for a very recent paper by Liu et al.<sup>20</sup>, which studied the effects of facets on  $\text{Cu}_2\text{O}$  micromotor motion.

Many studies are conducted with interest in the application of micromotors in combatting bacterial contamination. The abilities to produce motion and carry potential antibacterial compounds are promising tools for the combination of mechanical eradication and biochemical interactions between micromotors and bacterial biofilms<sup>21–25</sup>.

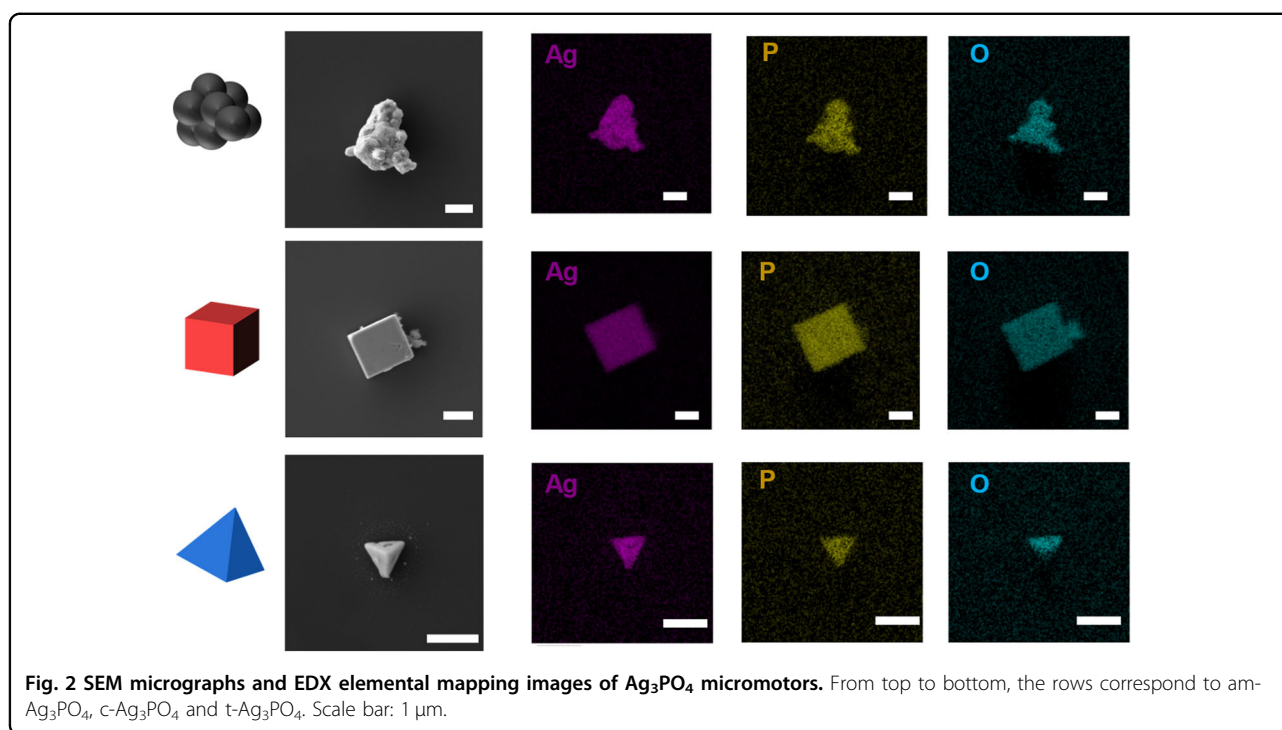
The ability of bacteria to form biofilms is a dangerous kind of virulence that causes threats in the surgery field (risk of gram-positive methicillin-resistant *Staphylococcus aureus* (MRSA) presence) and in the food industry, such as the dairy and meat industries (risk of gram-negative *Pseudomonas aeruginosa* (*P. aeruginosa*) presence)<sup>26</sup>. The removal of biofilms by commonly used sanitary compounds is impossible to conduct in hard-to-reach places. By combining the mechanical eradication of biofilms by micromotors with the cell death of biofilm bacteria, a modern and sophisticated method is facilitated for application in biofouling clean-up processes in many industries<sup>27</sup>.

Therefore, in this work, the effects of the presence of different exposed facets on the motion of visible-light driven  $\text{Ag}_3\text{PO}_4$  photocatalytic micromotors was evaluated. In addition, taking advantage of the antibacterial properties of  $\text{Ag}_3\text{PO}_4$ , their ability to eliminate the bacterial biofilms of *P. aeruginosa* and MRSA bacteria was observed in the absence of  $\text{H}_2\text{O}_2$  and UV light.

## Results and discussion

### Preparation and characterization of $\text{Ag}_3\text{PO}_4$ photocatalytic micromotors

The effects of different crystal facets on the photocatalytic properties of  $\text{Ag}_3\text{PO}_4$  have been studied in recent years to improve its performance in the photo-degradation of pollutants<sup>28,29</sup>, water splitting<sup>12,30,31</sup> and biofilm eradication<sup>32–34</sup>. Even if some reports in the literature were conducted with regard to the motion of  $\text{Ag}_3\text{PO}_4$ -based particles, only cubic and amorphous particles have been separately studied. However, the effects of different shapes and facets of different  $\text{Ag}_3\text{PO}_4$  particles remain unexplored. Therefore, the main objective of this work was to explore the effects of crystal facet engineering on  $\text{Ag}_3\text{PO}_4$ -based micromotor motion and antibiofilm properties (Fig. 1A). To investigate the relationships between facets and motion, different shapes of  $\text{Ag}_3\text{PO}_4$  micromotors were synthesized using a cheap and scalable precipitation method. Amorphous  $\text{Ag}_3\text{PO}_4$  (am- $\text{Ag}_3\text{PO}_4$ ) containing mixed facets, cubic  $\text{Ag}_3\text{PO}_4$  (c- $\text{Ag}_3\text{PO}_4$ ) with dominating {100} facets and tetrahedral  $\text{Ag}_3\text{PO}_4$  (t- $\text{Ag}_3\text{PO}_4$ ) with dominating {111} facets were synthesized. Am- $\text{Ag}_3\text{PO}_4$  was synthesized by the direct precipitation of  $\text{AgNO}_3$  with  $\text{NaH}_2\text{PO}_4$ , while in the case of c- $\text{Ag}_3\text{PO}_4$ , a silver/ammonia complex was formed before the addition of  $\text{NaH}_2\text{PO}_4$ . The motion mechanism for light-powered  $\text{Ag}_3\text{PO}_4$ -based nanocarriers is schematically illustrated in Fig. 1B. Visible light photons having energies equal to or higher than the  $\text{Ag}_3\text{PO}_4$  bandgap are absorbed, promoting electrons ( $e^-$ ) from the valence band (VB) to the conduction band (CB) and leaving holes in the VB. The energy of the holes created by visible light is sufficiently high to oxidize water, producing oxygen. However, the energy of the electrons is lower than that of  $\text{H}^+/\text{H}_2$ ; hence, without the addition of



an electron scavenger,  $\text{Ag}_3\text{PO}_4$  itself will decompose during water photooxidation, producing Ag on the surface and realizing the formation of  $\text{Ag}^+$  ions<sup>13,35</sup>. The asymmetric generation of chemical species on the surface of the  $\text{Ag}_3\text{PO}_4$  micromotors is mainly responsible for their motion<sup>15</sup>. Since the photogenerated ions diffuse at different rates, a local electric field is generated due to the asymmetric charge distribution around the motor, moving the particles forward due to a self-diffusiophoretic mechanism<sup>9,36</sup>. Due to the high activity of this reaction,  $\text{Ag}_3\text{PO}_4$  is able to display self-propulsion in fuel-free conditions in deionized water.

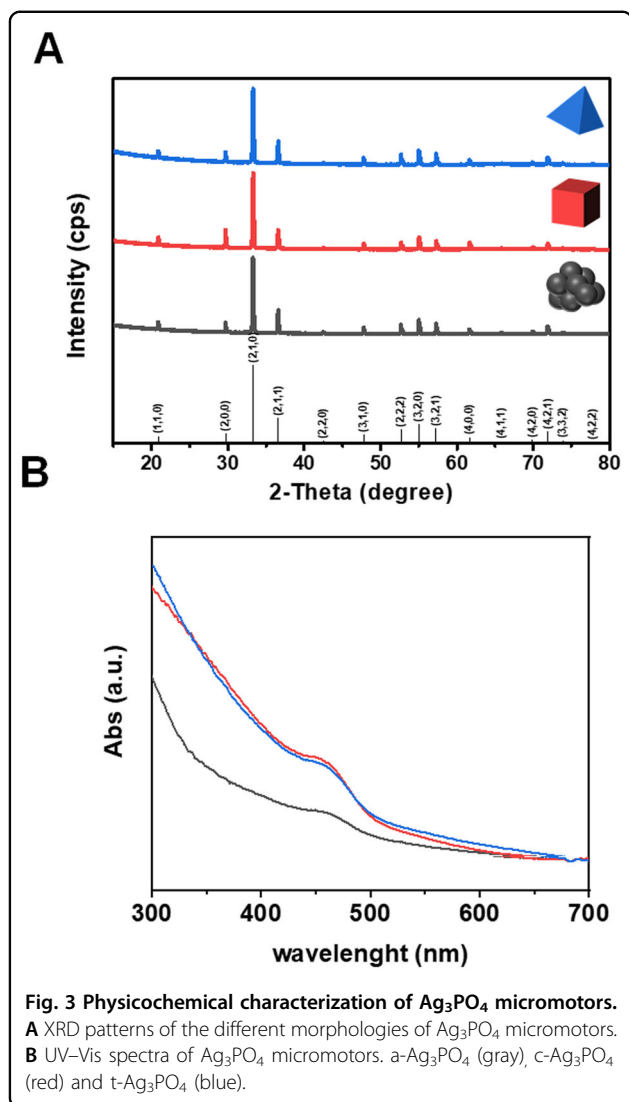
As seen in the micrographs shown in Fig. 2, the successful syntheses of am- $\text{Ag}_3\text{PO}_4$ , c- $\text{Ag}_3\text{PO}_4$  and t- $\text{Ag}_3\text{PO}_4$  were accomplished. Additionally, the EDS mapping confirmed the presence of the constituent elements Ag, P and O, confirming the particle composition. However, a larger cluster of particles retaining the shape and exposed facets were also observed, as shown in Fig. S1.

To confirm the dominating facets in the prepared samples, their XRD spectra were recorded and investigated. The X-ray diffraction patterns shown in Fig. 3A clearly indicate a full phase match with the body-centered cubic crystalline structure of  $\text{Ag}_3\text{PO}_4$  (6.004 Å, BCC, JCPDS no. 06-0505). No additional peaks were found in the XRD signals, indicating well-crystallized pure-phase compounds for all the structures and the absence of impurities. The c- $\text{Ag}_3\text{PO}_4$  showed an intensity ratio of 0.35 between the peaks of the {110} and {200} planes,

which is weaker than that in the am- $\text{Ag}_3\text{PO}_4$  (0.65) and t- $\text{Ag}_3\text{PO}_4$  (0.63) planes. This indicates the preferential exposure of {100} facets in c- $\text{Ag}_3\text{PO}_4$ . In addition, the ratio between the {222} and {200} planes is higher in the case of t- $\text{Ag}_3\text{PO}_4$  (1.20) than in the cases of am- $\text{Ag}_3\text{PO}_4$  (1.01) and c- $\text{Ag}_3\text{PO}_4$  (0.43). These ratios indicate the preferential exposure of {111} facets in t- $\text{Ag}_3\text{PO}_4$ <sup>30,37</sup>. The UV–vis spectra (UV–VIS) of the different particles are presented in Fig. 3B. All samples showed an absorption edge at approximately 500 nm, confirming their visible light absorption.

#### Motion behavior of $\text{Ag}_3\text{PO}_4$ photocatalytic micromotors

The motion of the different synthesized  $\text{Ag}_3\text{PO}_4$  micromotors can be observed in Videos S1 to S3 for t- $\text{Ag}_3\text{PO}_4$ , c- $\text{Ag}_3\text{PO}_4$  and am- $\text{Ag}_3\text{PO}_4$ , respectively. The particles were tracked using Trackmate, and the resulting trajectories were extracted and plotted from the coordinate origin of each particle (Fig. 4A). Particle movement was tracked over 10 s under dark and illuminated conditions using a visible light microscope source, and the track length was dramatically increased from the dark to the illuminated conditions, confirming the visible light-powered motion mechanism of the particles. The  $\text{Ag}_3\text{PO}_4$  micromotor trajectories were studied by performing mean-squared displacement (MSD) analysis under different dark and visible light irradiation conditions in deionized water. The MSD ( $\mu\text{m}^2$ ) for a given time interval ( $\Delta t$ ) is defined as follows, where  $\langle \rangle$  indicates an



assembly of  $n$  particles:

$$\langle MSD \rangle = (x(\Delta t) - x_0)^2 + (y(\Delta t) - y_0)^2 \quad (1)$$

In the case of pure Brownian motion, the MSD obeys the following relationship:

$$\langle MSD \rangle = 4D\Delta t \quad (2)$$

where  $D$  ( $\mu\text{m}^2\text{s}^{-1}$ ) is the diffusion coefficient of the particles.

In the case of ballistic motion, the MSD obeys the following relationship:

$$\langle MSD \rangle = 4D\Delta t + v^2\Delta t^2 \quad (3)$$

The time interval or frame rate used (50 FPS) was set below the rotational diffusion ( $\tau_R$ ), where ballistic motion dominates over rotational motion.  $\tau_R$  was calculated using the following equation:

$$\tau_R = \frac{8\pi\eta R^3}{k_B T} \quad (4)$$

where  $\eta$  is the viscosity (0.89 mPa),  $k_B$  is the Boltzmann constant,  $T$  is the temperature (25 °C) and  $R$  is the particle radius.  $\tau_R$  was estimated to be 13 s, and hence, the MSD was studied for  $t < 1$  s ( $t < \tau_R$ ). Under these conditions, the motion mechanisms of the  $\text{Ag}_3\text{PO}_4$ -based micromotors containing different facets were studied through their MSD analyses. Under dark conditions, the MSD values of all three structures increased linearly over time, indicating Brownian motion, whereas under visible light irradiation, increased parabolically, indicating ballistic motion (Fig. 4B). From the MSD fitting, the diffusion coefficients of the micromotors were calculated and are plotted in Fig. 4C. The mixed potential of a semiconductor under dark and light conditions provides information about the corresponding catalytic process. As seen in Fig. 4D, the mixed potential values of the different  $\text{Ag}_3\text{PO}_4$  micromotors were shifted toward more anodic potentials following the order of  $\Delta E_{\text{Ag}_3\text{PO}_4 \text{Light:dark}} = 73, 51$ , and  $29$  mV for t- $\text{Ag}_3\text{PO}_4$ , c- $\text{Ag}_3\text{PO}_4$  and a- $\text{Ag}_3\text{PO}_4$ , respectively. The positive shift in the mixed potential under irradiation indicates the tendency of the material to be reduced, which is associated with the photocorrosion of  $\text{Ag}_3\text{PO}_4$  into Ag, which is related to micromotor motion and  $\text{O}_2$  generation. Interestingly, these differences in the mixed potentials were correlated with the diffusion coefficients (D) of the  $\text{Ag}_3\text{PO}_4$  micromotors. Therefore, the trend found in the motion capability is in agreement with previous reports wherein {111} facets exhibited a higher photocatalytic activity than the {100} facets, confirming that we can tune the motion of  $\text{Ag}_3\text{PO}_4$  micromotors using faceting nanoarchitectonics<sup>30,37</sup>. Figure 5 shows the strong fluorescence exhibited by the  $\text{Ag}_3\text{PO}_4$ -based micromotors under 488 nm excitation. By taking advantage of their inherent fluorescence, the motors can also be tracked by fluorescence microscopy.

#### Biofilm eradication using $\text{Ag}_3\text{PO}_4$ photocatalytic micromotors

Our group's previous work studied the application of micromotors in targeting gram-positive and gram-negative biofilms. The motion of micromotors was induced by the presence of both 1 wt%  $\text{H}_2\text{O}_2$  and UV light exposure<sup>20</sup>. Despite the excellent eradication effect,  $\text{H}_2\text{O}_2$  at high concentrations and UV exposure are still

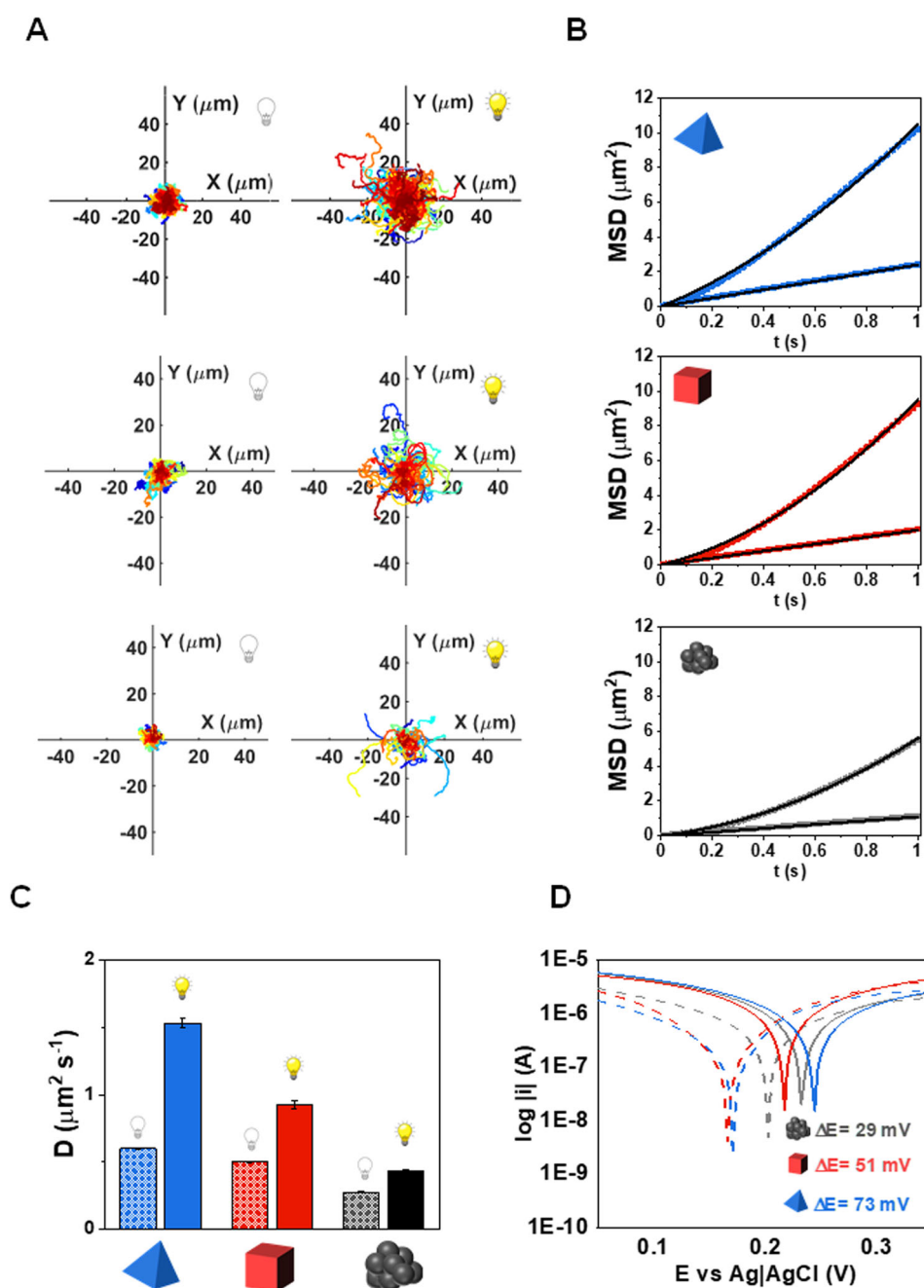


**Fig. 4** Motion characterization of  $\text{Ag}_3\text{PO}_4$  micromotors. **A** Groupings of the analyzed trajectories of  $\text{Ag}_3\text{PO}_4$  micromotors over 10 s plotted from a single origin under dark (lightbulb OFF) and visible illumination (lightbulb ON). **B** MSD values of  $\text{Ag}_3\text{PO}_4$  micromotors under dark conditions (squares) and visible light illumination (circles). Each row corresponds to a micromotor shape; from top to bottom: t- $\text{Ag}_3\text{PO}_4$ , c- $\text{Ag}_3\text{PO}_4$  and a- $\text{Ag}_3\text{PO}_4$ . **C** Diffusion coefficients calculated from MSD of t- $\text{Ag}_3\text{PO}_4$  (blue), c- $\text{Ag}_3\text{PO}_4$  (red) and a- $\text{Ag}_3\text{PO}_4$  (black). **D** Tafel plots of t- $\text{Ag}_3\text{PO}_4$  (blue), c- $\text{Ag}_3\text{PO}_4$  (red) and a- $\text{Ag}_3\text{PO}_4$  (black).

invasive for nontargeted bacteria and other surrounding organisms. In this study of micromotors, motion is induced by visible light along without the need for  $\text{H}_2\text{O}_2$ . The am- $\text{Ag}_3\text{PO}_4$ , c- $\text{Ag}_3\text{PO}_4$ , and t- $\text{Ag}_3\text{PO}_4$  micromotors were tested on two different bacterial monospecies

biofilms. The bacterial strains used for the biofilm eradication tests were gram-positive in the case of methicillin-resistant *Staphylococcus aureus* (MRSA) and gram-negative in the case of *Pseudomonas aeruginosa* (*P. aeruginosa*).



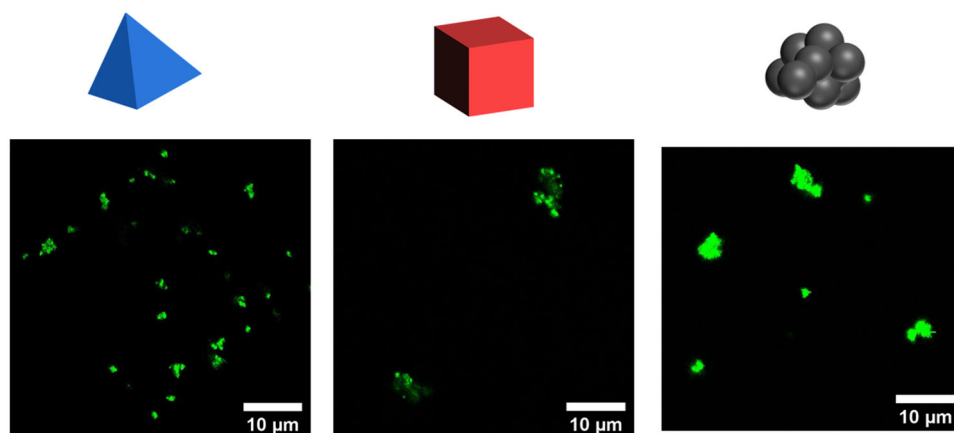


**Fig. 5** Fluorescence microscopy images of t- $\text{Ag}_3\text{PO}_4$ , c- $\text{Ag}_3\text{PO}_4$  and a- $\text{Ag}_3\text{PO}_4$  (from left to right) micromotors in pure water under light excitation ( $\lambda_{\text{exc}} = 488 \text{ nm}$ ). The light emitted by the particles was recorded at  $\lambda_{\text{em}} = 500\text{--}550 \text{ nm}$ .

Viability assays were performed under three different conditions: control (indicated as C, bacteria under light exposure), in the presence of static micromotors ( $1 \mu\text{g}/\text{mL}$ ) under dark conditions (S) and using the same amount of moving micromotors under light irradiation (M). As shown in Fig. 6A, the presence of micromotors dramatically affected biofilm viability, which was highly decreased in the presence of static micromotors (66%, 74% and 45% for am- $\text{Ag}_3\text{PO}_4$ , c- $\text{Ag}_3\text{PO}_4$ , and t- $\text{Ag}_3\text{PO}_4$ , respectively) and decreased to a greater extent under moving conditions (17%, 57% and 15% for am- $\text{Ag}_3\text{PO}_4$ , c- $\text{Ag}_3\text{PO}_4$ , and t- $\text{Ag}_3\text{PO}_4$ , respectively). In addition to biofilm viability, the influences of the micromotors on biofilm thickness were evaluated with positive results. The treatment of gram-negative *Pseudomonas aeruginosa* with all micromotor shapes resulted in significant decreases in biofilm thickness, from  $77 \mu\text{m}$  in the control to 45, 38, and 18% with respect to the control values for am- $\text{Ag}_3\text{PO}_4$ , c- $\text{Ag}_3\text{PO}_4$ , and t- $\text{Ag}_3\text{PO}_4$ , respectively (Fig. 6B). Additionally, the confocal microscope images of the biofilm shown in Fig. S4 indicate a sparser and weaker biofilm after treatment.

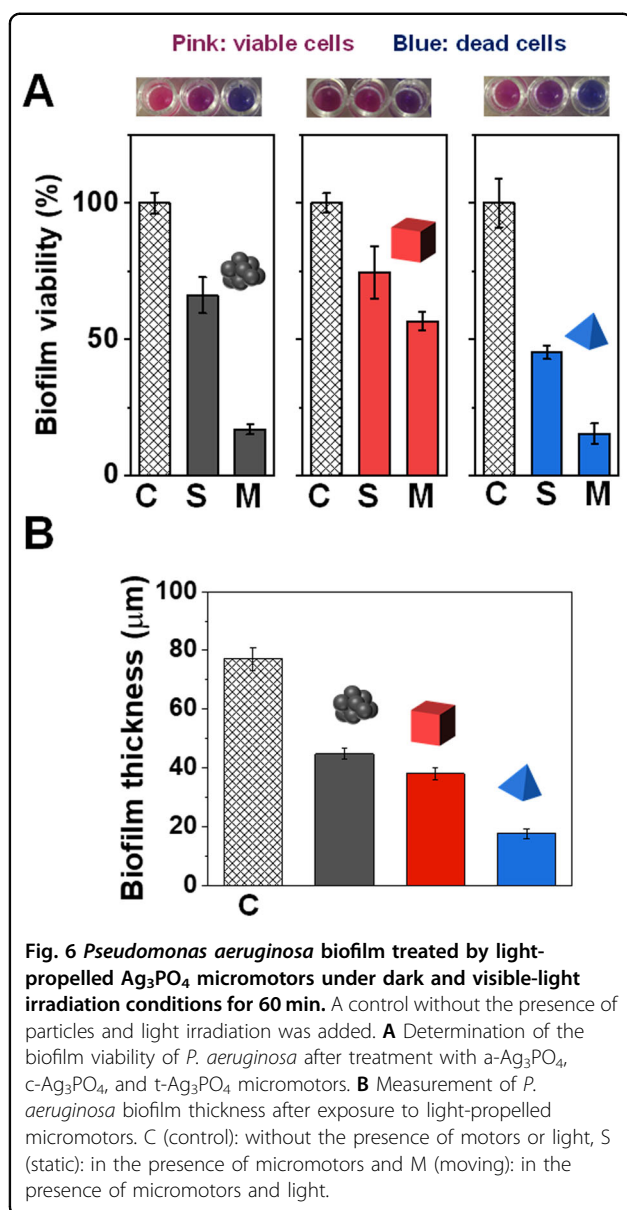
The treatment of the biofilm of methicillin-resistant *S. aureus* (MRSA) by micromotors was significantly more effective in comparison with that of *P. aeruginosa* biofilm. In this case, the viability assay, as shown in Fig. 7A, showed that in the presence of static micromotors, lower viability was recorded in comparison to that of *P. aeruginosa* (1%, 32% and 18% for am- $\text{Ag}_3\text{PO}_4$ , c- $\text{Ag}_3\text{PO}_4$ , and t- $\text{Ag}_3\text{PO}_4$ , respectively), which decreased to a greater extent under moving conditions (0.5%, 4% and 4% for am- $\text{Ag}_3\text{PO}_4$ , c- $\text{Ag}_3\text{PO}_4$ , and t- $\text{Ag}_3\text{PO}_4$ , respectively). The thickness of the biofilm also decreased in comparison to that of the control, from  $19 \mu\text{m}$  for the control to 9, 8 and  $13 \mu\text{m}$  for am- $\text{Ag}_3\text{PO}_4$ ,

c- $\text{Ag}_3\text{PO}_4$ , and t- $\text{Ag}_3\text{PO}_4$ , respectively. The biofilm again appeared sparser than the control (Fig. S5).

Differences in the effects on MRSA and *P. aeruginosa* are caused by the arrangement and composition of the biofilm matrix and by the molecular composition of the bacterial gram-positive and gram-negative cell walls. Previous reports, such as those in the study performed by Choi et al., mentioned that the pathogen autoaggregation ability of *S. aureus* is 2 times higher than that of *P. aeruginosa*. The reason for this may be the significantly higher ability of *P. aeruginosa* to produce proteins, carbohydrates, and eDNA in its biofilms compared to that of MRSA, which could explain the different efficiencies of biofilm eradication observed in this work<sup>38</sup>.

## Conclusions

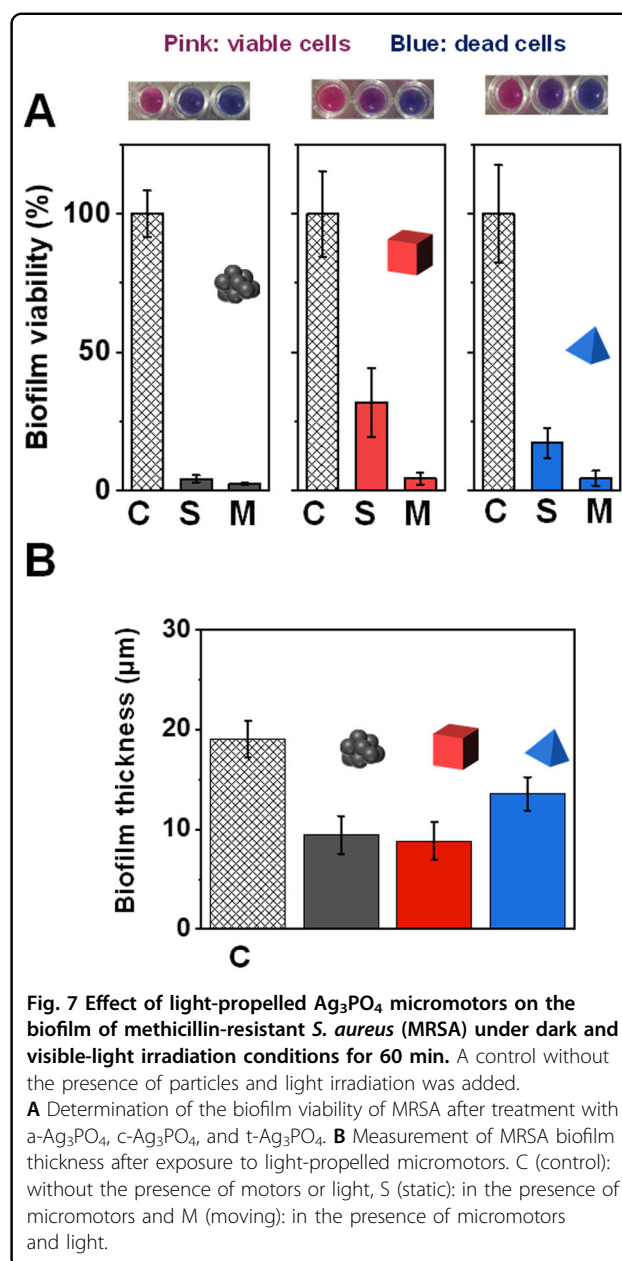
In this work, we developed fuel-free  $\text{Ag}_3\text{PO}_4$  micromotors powered by visible light irradiation. The  $\text{Ag}_3\text{PO}_4$ -based micromotors were synthesized with different exposed facets to study the corresponding effects on their motion. t- $\text{Ag}_3\text{PO}_4$  exhibited the highest motion capability, which is in accordance with its more active facets. Moreover, the  $\text{Ag}_3\text{PO}_4$ -based micromotors exhibited high inherent fluorescence, which can be advantageous for their tracking. Furthermore, the proposed  $\text{Ag}_3\text{PO}_4$ -based micromotors were employed for the biofilm eradication of gram-positive and gram-negative bacterial biofilms, demonstrating enhanced biofilm eradication under motion conditions compared with that under static conditions. These results show the potential of crystal facet engineering in the design of new micromotors for tuning their motion and also demonstrate the use of low-cost visible light-driven fuel-free photocatalytic-based micromotors as alternatives to other previously reported antibiofilm micromotors requiring the use of both UV light and  $\text{H}_2\text{O}_2$ .



## Material and methods

### Synthesis

Different  $\text{Ag}_3\text{PO}_4$  shapes were synthesized by a simple and scalable precipitation method as follows. For t- $\text{Ag}_3\text{PO}_4$ , 43 mg  $\text{AgNO}_3$  was added to a beaker containing 2 mL of ethanol to form a homogeneous solution. The solution was added dropwise to a reaction flask containing 10 mL of 0.1 M  $\text{H}_3\text{PO}_4$  ethanol solution at 60 °C, forming a precipitate. In the case of c- $\text{Ag}_3\text{PO}_4$ , the formation of the  $[\text{Ag}(\text{NH}_3)_2]^+$  complex was required prior to  $\text{Ag}_3\text{PO}_4$ . To achieve this, 100 mg  $\text{AgNO}_3$  was added to 10 mL deionized water, and 0.1 M ammonia solution was added dropwise. First, a dark precipitate of silver oxides appeared, which was further dissolved by adding an excess of  $\text{NH}_3$  to form the  $[\text{Ag}(\text{NH}_3)_2]^+$  complex. Then, 0.15 M



$\text{Na}_2\text{HPO}_4$  solution was added dropwise to the  $[\text{Ag}(\text{NH}_3)_2]^+$  solution to form a precipitate. For a- $\text{Ag}_3\text{PO}_4$ , 10 mL of 0.15 M  $\text{Na}_2\text{HPO}_4$  was added dropwise to 30 mL of 0.15 M  $\text{AgNO}_3$  to obtain a precipitate. The obtained yellow precipitates were collected by centrifugation and washed with deionized water and ethanol four times. Finally, the obtained powders were dried in an oven at 60 °C for 12 h<sup>37,39</sup>.

### Physicochemical characterization

A Tescan MIRA 3 XMU SEM equipped with an EDX detector (Oxford Instruments) was used for morphology characterization and elemental mapping. The crystallinity

was studied by X-ray diffraction (XRD) using an X-ray diffractometer (Rigaku SmartLab 3 kW) with a Bragg Bragg geometry and Cu K $\alpha$  radiation. UV–Vis spectra were recorded using a Jasco V-750 UV–Vis spectrophotometer.

### Electrochemical measurements

Prior to Tafel experiments, 5  $\mu$ L of a Ag<sub>3</sub>PO<sub>4</sub> suspension (1 mg mL<sup>−1</sup>) was dropcast onto a screen-printed electrode to produce a working electrode. An Ag/AgCl/0.1 M KCl electrode was used as a reference electrode, and a Pt wire was used as a counter electrode. Deionized water was used as an electrolyte to mimic the conditions of the movement experiments. Tafel plot measurements were carried out with an Autolab potentiostat (PGSTAT 204, Metrohm) with NOVA software 2.1 at a scan rate of 5 mV s<sup>−1</sup>. The irradiation source was a customized setup consisting of light-emitting diodes (LZ4-40B208, LedEngin Inc.) with a wavelength of 460 nm.

### Movement characterization

For the movement characterization, a-Ag<sub>3</sub>PO<sub>4</sub>, c-Ag<sub>3</sub>PO<sub>4</sub> and t-Ag<sub>3</sub>PO<sub>4</sub> dispersions at concentrations of 0.05 mg were placed on glass slides that were then observed using 40x and 60x objectives (Nikon ECLIPSE TS2R inverted microscope). Videos were recorded using a Hamamatsu digital C13440-20CU camera at a frame rate of 50 FPS. The light flux (160 mW/cm<sup>2</sup>) was determined by measuring the light power passing through the sample position (Optical power meter S305C, Thorlabs, USA). The recorded videos were tracked using the Trackmate plugin for ImageJ<sup>40</sup>, and MSD values were calculated using the msdanalyzer<sup>41</sup>.

### Biofilm eradication experiments

a-Ag<sub>3</sub>PO<sub>4</sub>, c-Ag<sub>3</sub>PO<sub>4</sub> and t-Ag<sub>3</sub>PO<sub>4</sub> were used for the elimination of monospecies bacterial biofilms. Gram-positive methicillin-resistant *S. aureus* (CCM 7110) and gram-negative *Pseudomonas aeruginosa* (CCM 3955) bacteria obtained from the Czech Collection of Microorganisms (CCM, Brno, Czech Republic) were tested for biofilm eradication in 96-well plates using the following protocol: Fresh bacterial culture was diluted in brain heart infusion broth (BHI) to an optical density of 0.1 (OD<sub>600</sub>), and 200  $\mu$ L of bacterial inoculum was pipetted into 96-well U-shaped plates for 7 days of incubation at 37 °C. The BHI medium was changed regularly every day. After incubation, the biofilm plates were washed three times with phosphate-buffered saline (PBS). Micromotors were used at a concentration of 1  $\mu$ g mL<sup>−1</sup>. The experiments were performed in four replicates, and error bars are expressed as the standard deviation. Plates with biofilm and micromotor samples were irradiated using an LED lamp (Fig. S3 for emission spectra) to enhance biofilm eradication ability, and the controls were prepared at the same time. Measurements of biofilm viability were

performed at 60 min, and then the biofilms were washed three times with PBS. Biofilm viability was determined by Alamar Blue staining (Thermo Fisher Scientific, Waltham, MA, USA) according to the manufacturer's instructions. The fluorescence of each well was evaluated (560/590 nm, excitation/emission). 3D biofilm images and thicknesses were collected using confocal scanning microscopy as described in our previous study<sup>20</sup>.

### Acknowledgements

This work was supported by the project Advanced Functional Nanorobots (reg. No. CZ.02.1.01/0.0/0.0/15\_003/0000444 financed by the EFRR). M.P. was also supported by Ministry of Education, Youth and Sports (Czech Republic) grant LL2002 under ERC CZ program. K.D. and M.K. acknowledge financial support from ERDF "Multidisciplinary research to increase application potential of nanomaterials in agricultural practice" (No. CZ.02.1.01/0.0/0.0/16\_025/0007314).

### Author details

<sup>1</sup>Future Energy and Innovation Laboratory, Central European Institute of Technology, Brno University of Technology (CEITEC-BUT), Purkyňova 123, 61200 Brno, Czech Republic. <sup>2</sup>Department of Chemistry and Biochemistry, Mendel University in Brno, Zemedelska 1, CZ-613 00 Brno, Czech Republic. <sup>3</sup>Department of Chemical and Biomolecular Engineering, Yonsei University, 50 Yonsei-ro, Seodaemun-Gu, Seoul 03722, South Korea. <sup>4</sup>Department of Medical Research, China Medical University Hospital, China Medical University, No. 91 Hsueh-Shih Road, Taichung 40402, Taiwan. <sup>5</sup>Center for Advanced Functional Nanorobots, Department of Inorganic Chemistry, University of Chemistry and Technology Prague, Technicka 5, 166 28 Prague, Czech Republic

### Author contributions

D.R. designed the experiments, synthesized the Ag<sub>3</sub>PO<sub>4</sub> micromotors, and performed SEM-EDX, XRD, UV–Vis, electrochemical measurements, and motion analysis. M.K. participated in biofilm preparation, treatment optimization, and the determination of biofilm viability. K.D. prepared and treated the biofilms for confocal microscopy and biofilm thickness measurements, supervised the design of the microbiological analyses and contributed to writing of the manuscript. M.P. conceptualized the research and supervised the micromotor-based work.

### Competing interests

The authors declare no competing interests.

### Publisher's note

Springer Nature remains neutral with regard to jurisdictional claims in published maps and institutional affiliations.

**Supplementary information** The online version contains supplementary material available at <https://doi.org/10.1038/s41427-022-00409-0>.

Received: 27 February 2022 Revised: 12 May 2022 Accepted: 1 June 2022.  
Published online: 29 July 2022

### References

- Yuan, K., Bujalance-Fernández, J., Jurado-Sánchez, B. & Escarpa, A. Light-driven nanomotors and micromotors: envisioning new analytical possibilities for biosensing. *Microchimica Acta*. **187**, 1–16 (2020).
- Maric, T., Nasir, M. Z. M., Webster, R. D. & Pummer, M. Tailoring Metal/TiO<sub>2</sub> Interface to Influence Motion of Light-Activated Janus Micromotors. *Adv. Funct. Mater.* **30**, 1908614 (2020).
- Dong, R., Zhang, Q., Gao, W., Pei, A. & Ren, B. Highly efficient light-driven TiO<sub>2</sub>–Au Janus micromotors. *ACS Nano*. **10**, 839–844 (2015).
- Pourahimi, A. M., Villa, K., Sofer, Z. & Pummer, M. Light-driven sandwich ZnO/TiO<sub>2</sub>/Pt Janus micromotors: Schottky barrier suppression by addition of TiO<sub>2</sub> atomic interface layers into ZnO/Pt micromachines leading to enhanced fuel-free propulsion. *Small Methods* **3**, 1900258 (2019).



5. Zhou, C., Zhang, H. P., Tang, J. & Wang, W. Photochemically powered AgCl Janus micromotors as a model system to understand ionic self-diffusiophoresis. *Langmuir* **34**, 3289–3295 (2018).
6. Wang, X., Baraban, L., Nguyen, A., Ge, J., Misko, V. R. & Tempere, et al. High-motility visible light-driven Ag/AgCl Janus micromotors. *Small* **14**, 1803613 (2018).
7. Wang, Q. et al. Glucose-fueled micromotors with highly efficient visible-light photocatalytic propulsion. *ACS Appl. Mater. Interfaces* **11**, 6201–6207 (2019).
8. Sun, Y. et al. Visible light-driven micromotor with incident-angle-controlled motion and dynamic collective behavior. *Langmuir* **37**, 180–187 (2021).
9. Villa, K. et al. Visible-light-driven single-component BiVO<sub>4</sub> micromotors with the autonomous ability for capturing microorganisms. *ACS. Nano* **13**, 8135–8145 (2019).
10. Kochergin, Y. S. et al. Multifunctional visible-light powered micromotors based on semiconducting sulfur- and nitrogen-containing donor–acceptor polymer. *Adv. Funct. Mater.* **30**, 2002701 (2020).
11. Villa, K., Palenzuela, C. L. M., Sofer, Z., Matějková, S. & Pumera, M. Metal-free visible-light photoactivated C<sub>3</sub>N<sub>4</sub> bubble-propelled tubular micromotors with inherent fluorescence and on/off capabilities. *ACS. Nano* **12**, 12482–12491 (2018).
12. Hasijs, V. et al. A strategy to develop efficient Ag<sub>3</sub>PO<sub>4</sub>-based photocatalytic materials toward water splitting: Perspectives and challenges. *Chem. Cat. Chem.* **13**, 2965–2987 (2021).
13. Altemose, A., Harris, A. J. & Sen, A. Autonomous formation and annealing of colloidal crystals induced by light-powered oscillations of active particles. *Chem.Sys. Chem.* **2**, e1900021 (2020).
14. Altemose, A. et al. Chemically controlled spatiotemporal oscillations of colloidal assemblies. *Angew. Chem. Int. Ed.* **56**, 7817–7821 (2017).
15. Chen, C. et al. Light-steered isotropic semiconductor micromotors. *Adv. Mater.* **29**, 1603374 (2017).
16. Asunción-Nadal, V., de la, Pacheco, M., Jurado-Sánchez, B. & Escarpa, A. Chalcogenides-based tubular micromotors in fluorescent assays. *Anal. Chem.* **92**, 9188–9193 (2020).
17. María-Hormigos, R. et al. Oscillatory light-emitting biopolymer based Janus microswimmers. *Adv. Mater. Interfaces* **7**, 1902094 (2020).
18. Pacheco, M., Jurado-Sánchez, B. & Escarpa, A. Visible-light-driven janus microvehicles in biological media. *Angew. Chem.* **131**, 18185–18192 (2019).
19. Urso, M., Ussia, M. & Pumera, M. Breaking polymer chains with self-propelled light-controlled navigable hematite microrobots. *Adv. Funct. Mater.* **31**, 2101510 (2021).
20. Liu, W. et al. Visible-light-driven cuprous oxide nanomotors with surface-heterojunction-induced propulsion. *Nanoscale Horiz.* **6**, 238–244 (2021).
21. Ussia, M. et al. Active light-powered antibiofilm ZnO micromotors with chemically programmable properties. *Adv. Funct. Mater.* **31**, 2101178 (2021).
22. Yuan, K., Jurado-Sánchez, B. & Escarpa, A. Dual-propelled antibiotic based janus micromotors for selective inactivation of bacterial biofilms. *Angew. Chem. Int. Ed.* **60**, 4915–4924 (2021).
23. Ge, Y. et al. Dual-fuel-driven bactericidal micromotor. *Nano-Micro Lett.* **8**, 157–164 (2015).
24. Delezuk, J. A. M., Ramírez-Herrera, D. E., Ávila, B. E-Fde & Wang, J. Chitosan-based water-propelled micromotors with strong antibacterial activity. *Nanoscale* **9**, 2195–2200 (2017).
25. Yuan, K., Jiang, Z., Jurado-Sánchez, B. & Escarpa, A. Nano/Micromotors for Diagnosis and Therapy of Cancer and Infectious Diseases. *Chem. – A Eur. J.* **26**, 2309–2326 (2020).
26. Cao, Y. et al. Non-antibiotic antimicrobial agents to combat biofilm-forming bacteria. *J. Glob. Antimicrobial Resistance* **21**, 445–451 (2020).
27. Shi, Z. et al. Rationally designed magnetic poly(catechol-hexanediamine) particles for bacteria removal and on-demand biofilm eradication. *Colloids Surf. B: Biointerfaces* **186**, 110728 (2020).
28. Ge, M., Zhu, N., Zhao, Y., Li, J. & Liu, L. Sunlight-assisted degradation of dye pollutants in Ag<sub>3</sub>PO<sub>4</sub> Suspension. *Ind. Eng. Chem. Res.* **51**, 5167–5173 (2012).
29. Teng, F., Liu, Z., Zhang, A. & Li, M. Photocatalytic performances of Ag<sub>3</sub>PO<sub>4</sub> polyods for degradation of dye pollutant under natural indoor weak light irradiation. *Environ. Sci. Technol.* **49**, 9489–9494 (2015).
30. Martin, D. J., Umezawa, N., Chen, X., Ye, J. & Tang, J. Facet engineered Ag<sub>3</sub>PO<sub>4</sub> for efficient water photooxidation. *Energy Environ. Sci.* **6**, 3380–3386 (2013).
31. He, G. et al. Facile controlled synthesis of Ag<sub>3</sub>PO<sub>4</sub> with various morphologies for enhanced photocatalytic oxygen evolution from water splitting. *RSC Adv.* **9**, 18222–18231 (2019).
32. Tran, H. A. & Tran, P. A. Immobilization-enhanced eradication of bacterial biofilms and in situ antimicrobial coating of implant material surface; an in vitro Study. *Int. J. Nanomed.* **14**, 9351–9360 (2019).
33. Steckiewicz, K. P. et al. Shape-Depended Biological Properties of Ag<sub>3</sub>PO<sub>4</sub> Microparticles: Evaluation of Antimicrobial Properties and Cytotoxicity in Vitro Model - Safety Assessment of Potential Clinical Usage. *Oxidative Med. Cellular Longevity* **2019**, 6740325 (2019).
34. Blanchette, V., Belosinschi, D., Lai, T. T., Cloutier, L. & Barnabé, S. New Anti-bacterial Paper Made of Silver Phosphate Cellulose Fibers: A Preliminary Study on the Elimination of Staphylococcus aureus Involved in Diabetic Foot Ulceration. *BioMed Res. Int.* **2020**, 1304016 (2020).
35. Yi, Z. et al. An orthophosphate semiconductor with photooxidation properties under visible-light irradiation. *Nat. Mater.* **9**, 559–564 (2010).
36. Hong, Y., Diaz, M., Córdova-Figueroa, U. M. & Sen, A. Light-Driven Titanium-Dioxide-Based Reversible Microfireworks and Micromotor/Micropump Systems. *Adv. Funct. Mater.* **20**, 1568–1576 (2010).
37. He, S. et al. Femtosecond time-resolved diffuse reflectance study on facet engineered charge-carrier dynamics in Ag<sub>3</sub>PO<sub>4</sub> for antibiotics photo-degradation. *Appl. Catal. B: Environ.* **281**, 119479 (2021).
38. Choi, N.-Y., Bae, Y.-M. & Lee, S.-Y. Cell surface properties and biofilm formation of pathogenic bacteria. *Food Sci. Biotechnol.* **24**, 2257–2264 (2015).
39. Bi, Y., Ouyang, S., Umezawa, N., Cao, J. & Ye, J. Facet effect of Single-Crystalline Ag<sub>3</sub>PO<sub>4</sub> Sub-microcrystals on photocatalytic properties. *J. Am. Chem. Soc.* **133**, 6490–6492 (2011).
40. Tinevez, J. Y. et al. TrackMate: An open and extensible platform for single-particle tracking. *Methods* **115**, 80–90 (2017).
41. Tarantino, N. et al. TNF and IL-1 exhibit distinct ubiquitin requirements for inducing NEMO-IKK supramolecular structures. *J. Cell Biol.* **204**, 231–245 (2014).